Efficient design of nanoplasmonic waveguide devices using the space mapping algorithm

Pouya Dastmalchi[1,2] **and Georgios Veronis**[1,2,*]

[1]*School of Electrical Engineering and Computer Science, Louisiana State University, Baton Rouge, Louisiana 70803, USA*

[2]*Center for Computation and Technology, Louisiana State University, Baton Rouge, Louisiana 70803, USA*

[*]*gveronis@lsu.edu*

Abstract: We show that the space mapping algorithm, originally developed for microwave circuit optimization, can enable the efficient design of nanoplasmonic waveguide devices which satisfy a set of desired specifications. Space mapping utilizes a physics-based coarse model to approximate a fine model accurately describing a device. Here the fine model is a full-wave finite-difference frequency-domain (FDFD) simulation of the device, while the coarse model is based on transmission line theory. We demonstrate that simply optimizing the transmission line model of the device is not enough to obtain a device which satisfies all the required design specifications. On the other hand, when the iterative space mapping algorithm is used, it converges fast to a design which meets all the specifications. In addition, full-wave FDFD simulations of only a few candidate structures are required before the iterative process is terminated. Use of the space mapping algorithm therefore results in large reductions in the required computation time when compared to any direct optimization method of the fine FDFD model.

OCIS codes: (240.6680) Surface plasmons; (260.3910) Metal optics; (130.2790) Guided waves.

References and links

1. W. L. Barnes, A. Dereux, and T. W. Ebbesen, "Surface plasmon subwavelength optics," Nature **424**, 824–830 (2003).
2. R. Zia, J. A. Schuller, A. Chandran, and M. L. Brongersma, "Plasmonics: the next chip-scale technology," Mater. Today **9**, 20–27 (2006).
3. E. Ozbay, "Plasmonics: Merging photonics and electronics at nanoscale dimensions," Science **311**, 189–193 (2006).
4. S. A. Maier and H. A. Atwater, "Plasmonics: localization and guiding of electromagnetic energy in metal/dielectric structures," J. Appl. Phys. **98**, 011101 (2005).
5. J. A. Schuller, E. S. Barnard, W. S. Cai, Y. C. Yun, J. S. White, and M. L. Brongersma, "Plasmonics for extreme light concentration and manipulation," Nat. Mater. **9**, 193–204 (2010).
6. D. K. Gramotnev and S. I. Bozhevolnyi, "Plasmonics beyond the diffraction limit," Nat. Photonics **4**, 83–91 (2010).
7. G. Veronis and S. Fan, "Theoretical investigation of compact couplers between dielectric slab waveguides and two-dimensional metal-dielectric-metal plasmonic waveguides," Opt. Express **15**, 1211–1221 (2007).
8. C. Min, L. Yang, and G. Veronis, "Microcavity enhanced optical absorption in subwavelength slits," Opt. Express **19**, 26850–26858 (2011).

#200639 - $15.00 USD Received 4 Nov 2013; revised 5 Dec 2013; accepted 10 Dec 2013; published 18 Dec 2013

9. T. Tanemura, K. C. Balram, D.-S. Ly-Gagnon, P. Wahl, J. S. White, M. L. Brongersma, and D. A. B. Miller, "Multiple-wavelength focusing of surface plasmons with a nonperiodic nanoslit coupler," Nano Lett. **11**, 2693–2698 (2011).
10. R. M. Briggs, J. Grandidier, S. P. Burgos, E. Feigenbaum, and H. A. Atwater, "Efficient coupling between dielectric-loaded plasmonic and silicon photonic waveguides," Nano Lett. **10**, 4851–4857 (2010).
11. C. Delacour, S. Blaize, P. Grosse, J. M. Fedeli, A. Bruyant, R. Salas-Montiel, G. Lerondel, and A. Chelnokov, "Efficient directional coupling between silicon and copper plasmonic nanoslot waveguides: toward metal-oxide-silicon nanophotonics," Nano Lett. **10**, 2922–2926 (2010).
12. G. Veronis and S. Fan, "Bends and splitters in subwavelength metal-dielectric-metal plasmonic waveguides," Appl. Phys. Lett. **87**, 131102 (2005).
13. G. Veronis, Z. Yu, S. E. Kocabas, D. A. B. Miller, M. L. Brongersma, and S. Fan, "Metal-dielectric-metal plasmonic waveguide devices for manipulating light at the nanoscale," Chin. Opt. Lett. **7**, 302–308 (2009).
14. J. W. Bandler, R. M. Biernacki, S. H. Chen, R. H. Hemmers, and K. Madsen, "Electromagnetic optimization exploiting aggressive space mapping," IEEE Trans. Microwave Theory Tech. **43**, 2874–2882 (1995).
15. J. W. Bandler, Q. S. Cheng, A. S. Dakroury, A. S. Mohamed, M. H. Bakr, K. Madsen, and J. Søndergaard, "Space mapping: The state of the art," IEEE Trans. Microwave Theory Tech. **52**, 337–360 (2004).
16. S. Koziel, Q. S. Cheng, and J. W. Bandler, "Space mapping," IEEE Microwave Mag. **9**, 105–122 (2008).
17. C. G. Broyden, "A class of methods for solving nonlinear simultaneous equations," Math. Comput. **19**, 577–593 (1965).
18. P. Huber, *Robust Statistics* (Wiley, 1981).
19. J. W. Bandler, S. H. Chen, R. M. Biernacki, L. Gao, K. Madsen, and H. Yu, "Huber optimization of circuits: A robust approach," IEEE Trans. Microwave Theory Tech. **41**, 2279–2287 (1993).
20. S. D. Wu and E. N. Glytsis, "Finite-number-of-periods holographic gratings with finite-width incident beams: analysis using the finite-difference frequency-domain method," J. Opt. Soc. Am. A **19**, 2018–2029 (2002).
21. G. Veronis, R. W. Dutton, and S. Fan, "Method for sensitivity analysis of photonic crystal devices," Opt. Lett. **29**, 2288–2290 (2004).
22. E. D. Palik, *Handbook of Optical Constants of Solids* (Academic, 1985).
23. J. Jin, *The Finite Element Method in Electromagnetics* (Wiley, 2002).
24. A. Taflove, *Computational Electrodynamics* (Artech House, 1995).
25. Y. Huang, C. Min, and G. Veronis, "Subwavelength slow-light waveguides based on a plasmonic analogue of electromagnetically induced transparency," Appl. Phys. Lett. **99**, 143117 (2011).
26. D. M. Pozar, *Microwave Engineering* (Wiley, 1998).
27. C. Min and G. Veronis, "Absorption switches in metal-dielectric-metal plasmonic waveguides," Opt. Express **17**, 10757–10766 (2009).
28. Y. Huang, C. Min, L. Yang, and G. Veronis, "Nanoscale plasmonic devices based on metal-dielectric-metal stub resonators," Int. J. Opt. **2012**, 372048 (2012).
29. S. E. Kocabas, G. Veronis, D. A. B. Miller, and S. Fan, "Transmission line and equivalent circuit models for plasmonic waveguide components," IEEE J. Sel. Top. Quantum Electron. **14**, 1462–1472 (2008).
30. D. Pacifici, H. J. Lezec, H. A. Atwater, and J. Weiner, "Quantitative determination of optical transmission through subwavelength slit arrays in Ag films: Role of surface wave interference and local coupling betwen adjacent slits," Phys. Rev. B **77**, 115411 (2008).
31. D. Pacifici, H. J. Lezec, L. A. Sweatlock, R. J. Walters, and H. A. Atwater, "Universal optical transmission features in periodic and quasiperiodic hole arrays," Opt. Express **16**, 9222–9238 (2008).
32. K. Krishnakumar, "Micro-genetic algorithms for stationary and non-stationary function optimization," Proc. SPIE **1196**, 289–296 (1989).
33. J. Tao, X. Huang, X. Lin, Q. Zhang, and X. Jin, "A narrow band subwavelength plasmonic waveguide filter with asymmetrical multiple-teeth-shaped structure," Opt. Express **17**, 13989–13994 (2009).
34. R. E. Collin, *Foundations for Microwave Engineering* (McGraw-Hill, 1966).
35. N. Engheta, "Circuits with light at nanoscales: Optical nanocircuits inspired by metamaterials," Science **317**, 1698–1702 (2007).
36. A. Alù, M. E. Young, and N. Engheta, "Design of nano filters for optical nanocircuits," Phys. Rev. B **77**, 144107 (2008).
37. H. Nejati and A. Beirami, "Theoretical analysis of the characteristic impedance in metal-insulator-metal plasmonic transmission lines," Opt. Lett. **37**, 1050–1052 (2012).
38. D. Li and E.-P. Li, "Impedance calculation and equivalent circuits for metal-insulator-metal plasmonic waveguide geometries," Opt. Lett. **38**, 3384–3386 (2013).
39. S. Koziel, J. W. Bandler, and K. Madsen, "Space mapping with adaptive response correction for microwave design optimization," IEEE Trans. Microwave Theory Tech. **57**, 478–486 (2009).
40. W. Shin, W. Cai, P. B. Catrysse, G. Veronis, M. L. Brongersma, and S. Fan, "Broadband sharp 90-degree bends and t-splitters in plasmonic coaxial waveguides," Nano Lett. **13**, 4753–4758 (2013).

#200639 - $15.00 USD Received 4 Nov 2013; revised 5 Dec 2013; accepted 10 Dec 2013; published 18 Dec 2013

1. Introduction

The unique properties of surface plasmons could enable a wide range of applications for plasmonics, including light guiding and manipulation at the nanoscale [1–6]. The realization of active and passive nanoplasmonic devices with optimal performance for high-density optical information processing could have profound implications for computing and communications. In designing such nanoplasmonic devices, ideally one would like to solve inverse problems starting from design specifications imposed on the device response. This can be achieved by combining global optimization algorithms with electromagnetic simulations [7, 8]. Such an approach leads to an extremely powerful design technique which can enable high performance nanoplasmonic devices. In many cases, the highly efficient device designs coming out of this approach cannot be obtained with any conventional design method based on analytical techniques [9]. However, integrated nanoplasmonic devices consist of multiple components and therefore have several design parameters [10, 11]. Thus, the solution of inverse problems by combining global optimization algorithms with electromagnetic simulations often requires simulation of hundreds to thousands of candidate structures before a design which satisfies all the specifications is reached. In most cases, full-wave electromagnetic simulation methods are too computationally expensive for this purpose. Thus, alternative approaches to solve inverse design problems for nanoplasmonic devices need to be explored.

In this paper, we show that the space mapping algorithm, originally developed for microwave circuit optimization, can enable the efficient design of nanoplasmonic devices which satisfy a set of desired specifications. Space mapping utilizes a physics-based coarse model to approximate a fine model accurately describing a device. The main concept in the algorithm is to find a mapping that relates the fine and coarse model design parameters. If such a mapping is established, we can then avoid directly optimizing the computationally expensive fine model during the design process. Instead, we perform optimization of the computationally efficient coarse model, and then use the mapping to find the corresponding fine model design.

More specifically, in this paper we demonstrate the use of the space mapping algorithm for the design of metal-dielectric-metal (MDM) plasmonic waveguide devices. Such devices could be potentially important in providing an interface between conventional optics and subwavelength electronic and optoelectronic devices [12, 13]. In our case, the fine model is a full-wave finite-difference frequency-domain (FDFD) simulation of the device, while the coarse model is based on transmission line theory. Through several examples, we demonstrate that simply optimizing the transmission line model of the device is not enough to obtain a device which satisfies all the required design specifications. On the other hand, we show that, when the iterative space mapping algorithm is used, it converges fast to a design which meets all the specifications. In addition, full-wave FDFD simulations of only a few candidate structures are required before the iterative process is terminated. Use of the space mapping algorithm therefore results in large reductions in the required computation time when compared to any direct optimization method of the fine FDFD model.

The remainder of the paper is organized as follows. In Section 2, we describe the space mapping algorithm used in this paper for the design of nanoplasmonic waveguide devices. In Section 3, we present several examples of the application of the algorithm for the design of such devices. Finally, our conclusions are summarized in Section 4.

2. Algorithm

Space mapping utilizes a physics-based coarse model to approximate a fine model which accurately describes a device [14–16]. The coarse and fine model design parameters are denoted by $\mathbf{x}_c$ and $\mathbf{x}_f$, respectively, while the corresponding responses are denoted by R_c and R_f. In this work it is assumed that $\mathbf{x}_c$ and $\mathbf{x}_f$ have the same dimensionality. In other words, the number

#200639 - $15.00 USD Received 4 Nov 2013; revised 5 Dec 2013; accepted 10 Dec 2013; published 18 Dec 2013

of design parameters n is the same for both models.The main concept in the space mapping algorithm is to find a mapping $\mathbf{P}$ that relates the fine and coarse model parameters through

$$\mathbf{x}_c = \mathbf{P}(\mathbf{x}_f), \tag{1}$$

such that

$$R_c(\mathbf{P}(\mathbf{x}_f)) \simeq R_f(\mathbf{x}_f). \tag{2}$$

We assume that such a one-to-one mapping exists in the region of interest. If such a mapping is established, we can then avoid using the direct optimization of the computationally expensive fine model to find the solution $\mathbf{x}_f^*$. Instead, we perform optimization of the computationally efficient coarse model to find its optimal solution $\mathbf{x}_c^*$, and then use

$$\bar{\mathbf{x}}_f \equiv \mathbf{P}^{-1}(\mathbf{x}_c^*) \tag{3}$$

to find an estimate of the fine model solution $\mathbf{x}_f^*$.

2.1. Aggressive space mapping

More specifically, here we use the aggressive space mapping implementation of the algorithm [14], which incorporates a quasi-Newton iteration. In this approach we assume that $\mathbf{x}_c$ is a nonlinear vector function $\mathbf{P}$ of $\mathbf{x}_f$ [Eq. (1)].

In the first step, we perform optimization of the computationally efficient coarse model and find its optimal solution $\mathbf{x}_c^*$. Eq. (3) can be rewritten as

$$\mathbf{P}(\bar{\mathbf{x}}_f) - \mathbf{x}_c^* = 0. \tag{4}$$

Thus, the solution of the space mapping algorithm $\bar{\mathbf{x}}_f$ can be found by solving the system of nonlinear equations

$$\mathbf{g}(\mathbf{x}_f) = 0, \tag{5}$$

where

$$\mathbf{g}(\mathbf{x}_f) \equiv \mathbf{P}(\mathbf{x}_f) - \mathbf{x}_c^*. \tag{6}$$

We can therefore use a quasi-Newton iterative method to solve this problem. Since the Jacobian matrix corresponding to Eq. (5)

$$\mathbf{J}(\mathbf{x}_f) = \left[\frac{\partial^T \mathbf{g}(\mathbf{x}_f)}{\partial \mathbf{x}_f}\right]^T \tag{7}$$

cannot be directly calculated, we use an approximation for the Jacobian matrix based on the Broyden formula [14, 17].

The initial point for the algorithm is the optimal solution of the coarse model $\mathbf{x}_c^*$

$$\mathbf{x}_f^{(1)} = \mathbf{x}_c^*. \tag{8}$$

If $\mathbf{x}_f^{(j)}$ is the jth approximation to the solution of Eq. (5) then $\mathbf{x}_f^{(j+1)}$ is found by

$$\mathbf{x}_f^{(j+1)} = \mathbf{x}_f^{(j)} + \mathbf{h}^{(j)}, \tag{9}$$

where $\mathbf{h}^{(j)}$ is the solution of the following linear system

$$\mathbf{B}^{(j)}\mathbf{h}^{(j)} = -\mathbf{g}^{(j)}. \tag{10}$$

#200639 - $15.00 USD Received 4 Nov 2013; revised 5 Dec 2013; accepted 10 Dec 2013; published 18 Dec 2013

In the above equation $\mathbf{g}^{(j)}$ is obtained by

$$\mathbf{g}^{(j)} \equiv \mathbf{g}(\mathbf{x}_f^{(j)}) = \mathbf{P}(\mathbf{x}_f^{(j)}) - \mathbf{x}_c^*, \tag{11}$$

where $\mathbf{P}(\mathbf{x}_f^{(j)})$ is calculated using the parameter extraction procedure described below, while $\mathbf{B}^{(j)}$ is obtained by the Broyden formula [17]

$$\mathbf{B}^{(1)} = \mathbf{I}, \tag{12}$$

$$\mathbf{B}^{(j)} = \mathbf{B}^{(j-1)} + \frac{\mathbf{g}^{(j)}\mathbf{h}^{(j-1)^T}}{\mathbf{h}^{(j-1)^T}\mathbf{h}^{(j-1)}}. \tag{13}$$

The iterative procedure is terminated after M iterations when the fine model response $R_f(\mathbf{x}_f^{(M)})$ satisfies the set of desired specifications.

2.2. Parameter extraction

At each iteration of the space mapping algorithm we use a parameter extraction procedure to obtain the mapping $\mathbf{x}_c = \mathbf{P}(\mathbf{x}_f)$ which corresponds to the optimum match between the coarse and fine model responses. More specfically, we use an optimization algorithm in combination with the coarse model of the structure to minimize the objective function $H(\mathbf{x}_c)$

$$\min_{\mathbf{x}_c} H(\mathbf{x}_c), \tag{14}$$

where

$$H(\mathbf{x}_c) = \sum_{i=1}^{n} \rho_k(e_i(\mathbf{x}_c)). \tag{15}$$

Here, e_i is the error at frequency ω_i, defined as the difference between the responses calculated with the coarse and fine models

$$e_i(\mathbf{x}_c) \equiv R_c(\mathbf{x}_c, \omega_i) - R_f(\mathbf{x}_f, \omega_i), \tag{16}$$

and $\rho_k(e_i)$ is the Huber norm [18, 19] given by

$$\rho_k(e_i) \equiv \begin{cases} e_i^2/2 & \text{, if } |e_i| \le k \\ k|e_i| - k^2/2 & \text{, if } |e_i| > k \end{cases}. \tag{17}$$

The Huber norm is robust against large errors e_i [14]. Here we use $k = 0.04$.

2.3. Application of the space mapping algorithm to design of nanoplasmonic waveguide devices

In this paper, we demonstrate the use of the space mapping algorithm for the design of nanoplasmonic waveguide devices. We assume that a set of desired specifications are imposed on the transmission response of the device. We wish to find the design parameters of the device so that its transmission response satisfies all the specifications. In our case, the fine model is a full-wave finite-difference frequency-domain (FDFD) simulation of the device [20, 21]. This method allows us to directly use experimental data for the frequency-dependent dielectric constant of metals such as silver [22], including both the real and imaginary parts, with no approximation. Perfectly matched layer (PML) absorbing boundary conditions are used at all boundaries of

#200639 - $15.00 USD Received 4 Nov 2013; revised 5 Dec 2013; accepted 10 Dec 2013; published 18 Dec 2013

the simulation domain [23, 24]. We use a fine spatial grid size in FDFD to ensure the convergence of the numerical results. Thus the fine FDFD model gives essentially the exact solution of the Maxwell's equations for the given device and therefore accurately describes the device. The coarse model is based on transmission line theory and will heretofore be referred to as the transmission line model of the device.

In our case the fine model design parameters are a set of geometric dimensions $\mathbf{L} = [L_1 \quad L_2 \quad \cdots \quad L_n]^T$ of the plasmonic device. The coarse transmission line model parameters have a one-to-one corespondence to the fine model parameters and are denoted as $\mathbf{L}_{\mathrm{TL}} = [L_{\mathrm{TL1}} \quad L_{\mathrm{TL2}} \quad \cdots \quad L_{\mathrm{TLn}}]^T$. The fine and coarse model responses are the transmission of the plasmonic device calculated with FDFD, T_{FDFD}, and the transmission line model, T_{TL}, respectively.

3. Results

In this section, we present several examples of the application of the space mapping algorithm for the design of nanoplasmonic waveguide devices.

3.1. MDM waveguide side-coupled to two MDM stub resonators

In the first example, the structure considered consists of a plasmonic MDM waveguide side-coupled to two MDM stub resonators [Fig. 1(a)]. The fundamental TM mode of the MDM waveguide is incident from the left. This system is a plasmonic analogue of electromagnetically-induced transparency (EIT) [25].

Using such a waveguide device geometry, we wish to design a structure with a bandpass filter response. More specifically, the design specifications imposed on the transmission response T of the structure are

$$T > 0.75 \quad \text{for} \quad 180\ \text{THz} < f < 200\ \text{THz}, \tag{18a}$$

$$T < 0.2 \quad \text{for} \quad 130\ \text{THz} < f < 160\ \text{THz} \quad \text{and} \quad 240\ \text{THz} < f < 270\ \text{THz}, \tag{18b}$$

where f is the frequency. The specifications are indicated in Figs. 1(c) and 1(d) with solid red lines. Here the design parameters are the lengths of the stub resonators L_1 and L_2, while the width w of all waveguide sections is fixed at $w = 50$ nm.

Based on transmission line theory, the transmission line model of this structure consists of two short-circuited transmission line resonators of lengths L_{TL1} and L_{TL2}, propagation constant γ, and characteristic impedance Z, which are connected in series to a transmission line with the same propagation constant γ and characteristic impedance Z [26, 27] [Fig. 1(b)]. The characteristic impedance is given by [12, 27]

$$Z = \frac{\gamma}{j\omega\varepsilon} w, \tag{19}$$

where $\omega = 2\pi f$, $j = \sqrt{-1}$, and ε is the dielectric permittivity of the dielectric region of the MDM waveguide. Based on transmission line theory, the transmission line model response $T_{\mathrm{TL}}(L_{\mathrm{TL1}}, L_{\mathrm{TL2}})$ of the structure of Fig. 1(a) can be calculated as [26, 28]

$$T_{\mathrm{TL}}(L_{\mathrm{TL1}}, L_{\mathrm{TL2}}) = \left| 1 + \frac{1}{2} \left[\tanh(\gamma L_{\mathrm{TL1}}) + \tanh(\gamma L_{\mathrm{TL2}}) \right] \right|^{-2}. \tag{20}$$

The transmission line model is computationally efficient with a required computation time which is negligible compared to a full-wave FDFD simulation of the device. However, the

#200639 - $15.00 USD Received 4 Nov 2013; revised 5 Dec 2013; accepted 10 Dec 2013; published 18 Dec 2013

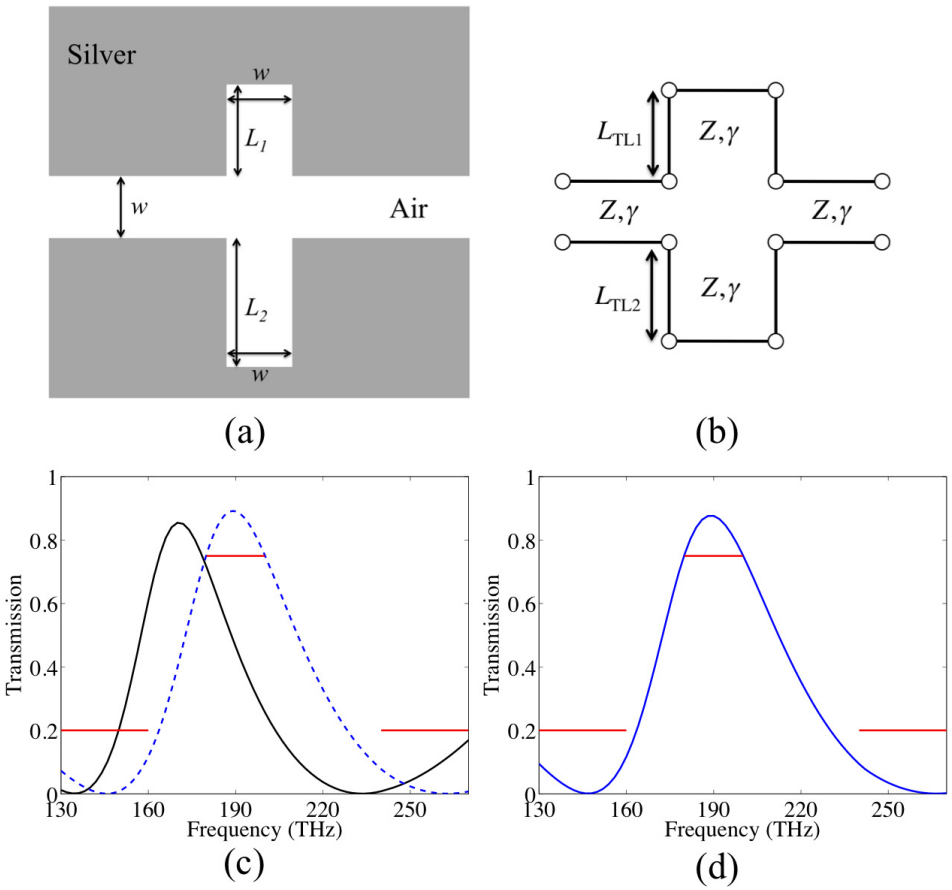

Fig. 1. (a) Schematic of a MDM plasmonic waveguide side-coupled to two MDM stub resonators. (b) Schematic of the transmission line model for the structure of Fig. 1(a). Here $Z(\omega)$ and $\gamma(\omega)$ are the characteristic impedance and complex propagation constant of the fundamental TM mode of a silver-air-silver plasmonic waveguide with width w. (c) Transmission line model response $T_{\mathrm{TL}}(L^*_{\mathrm{TL1}}, L^*_{\mathrm{TL2}})$ of the structure of Fig. 1(a) for parameters $L^*_{\mathrm{TL1}} = 210$ nm and $L^*_{\mathrm{TL2}} = 384$ nm obtained by optimizing the transmission line model of Fig. 1(b) (dashed blue line). We also show the transmission response calculated using FDFD, $T_{\mathrm{FDFD}}(L_1 = L^*_{\mathrm{TL1}}, L_2 = L^*_{\mathrm{TL2}})$ for the same parameters (solid black line). Results are shown for $w = 50$ nm. The red lines are the design specifications imposed on the transmission response of this structure. (d) Transmission response $T_{\mathrm{FDFD}}(\bar{L}_1, \bar{L}_2)$ of the structure of Fig. 1(a) calculated with FDFD for the parameters $\bar{L}_1 = 180$ nm and $\bar{L}_2 = 351$ nm obtained by the space mapping algorithm.

accuracy of this model is limited. The accuracy limitations of the transmission line model for circuits of MDM plasmonic waveguides have been described in detail elsewhere [29]. As an example, the transmission line model introduces errors in the phase of the reflection coefficient at the two interfaces of a side-coupled MDM stub resonator [30, 31].

We use the coarse transmission line model of the structure (without space mapping) in combination with a genetic global optimization algorithm [7, 32] to find the stub lengths L_{TL1} and L_{TL2} such that the transmission line model response $T_{\mathrm{TL}}(L_{\mathrm{TL1}}, L_{\mathrm{TL2}})$ satisfies the design specifications. During the optimization process the transmission line model response is calculated

#200639 - $15.00 USD Received 4 Nov 2013; revised 5 Dec 2013; accepted 10 Dec 2013; published 18 Dec 2013

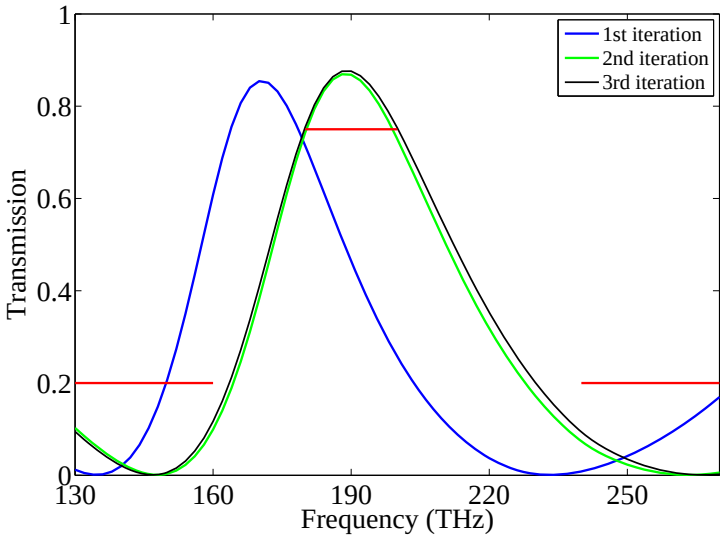

Fig. 2. Transmission response $T_{\text{FDFD}}(L_1^{(j)},L_2^{(j)})$ of the structure of Fig. 1(a) calculated with FDFD for parameters obtained after the jth iteration of the space mapping algorithm. $L_1^{(j)},L_2^{(j)}$ for $j=1,2,3$ are given in Table 1. All other parameters are as in Fig. 1(c).

at a discrete set of frequencies in the passband $(180\ \text{THz} < f < 200\ \text{THz})$ and stopbands $(130\ \text{THz} < f < 160\ \text{THz} \quad \text{and} \quad 240\ \text{THz} < f < 270\ \text{THz})$ for each structure. The objective is to maximize the transmission T_{TL} in the passband, and minimize it in the stopbands. The optimal transmission line model stub lengths found using this approach are $L^*_{\text{TL1}} = 210$ nm and $L^*_{\text{TL2}} = 384$ nm. As shown in Fig. 1(c), the transmission line model response for the optimized device $T_{\text{TL}}(L^*_{\text{TL1}},L^*_{\text{TL2}})$ (dashed blue line) meets all the design specifications [Eq. (18)].

We first investigate whether optimizing the transmission line model of the structure is enough to obtain a device which satisfies all the design specifications. We therefore perform a full-wave FDFD simulation of the device setting the stub lengths L_1, L_2 equal to the optimal transmission line model stub lengths, and obtain the device response $T_{\text{FDFD}}(L_1 = L^*_{\text{TL1}}, L_2 = L^*_{\text{TL2}})$. We observe that the transmission response of the device obtained with this approach $T_{\text{FDFD}}(L_1 = L^*_{\text{TL1}}, L_2 = L^*_{\text{TL2}})$ (black solid line) is substantially different from the transmission line model response $T_{\text{TL}}(L^*_{\text{TL1}},L^*_{\text{TL2}})$ (dashed blue line), and does not meet all the desired specifications [Fig. 1(c)]. This is due to the limited accuracy of the transmission line model which was discussed above. Thus, simply optimizing the transmission line model of the device is not enough to obtain a device which satisfies all the required design specifications.

To obtain such a device which will satisfy all the design specifications, we now use the space mapping algorithm, described in Section 2. We found that the space mapping algorithm converges fast to the design $\bar{L}_1 = 180$ nm and $\bar{L}_2 = 351$ nm with device response $T_{\text{FDFD}}(\bar{L}_1,\bar{L}_2)$, which meets all the specifications [Fig. 1(d)]. The initial point for the algorithm is the optimal solution of the coarse transmission line model [Eq. (8)]

$$[L_1^{(1)} \quad L_2^{(1)}]^T = [L^*_{\text{TL1}} \quad L^*_{\text{TL2}}]^T = [210\ \text{nm} \quad 384\ \text{nm}]^{\text{T}}. \tag{21}$$

We then follow the iterative process described in Section 2.1. At each step of the algorithm the next approximation to the solution is found using Equations (9) and (10). The design parameters $L_1^{(j)}$, $L_2^{(j)}$ found after the jth iteration of the algorithm are shown in Table 1. Figure 2 shows the

#200639 - $15.00 USD Received 4 Nov 2013; revised 5 Dec 2013; accepted 10 Dec 2013; published 18 Dec 2013

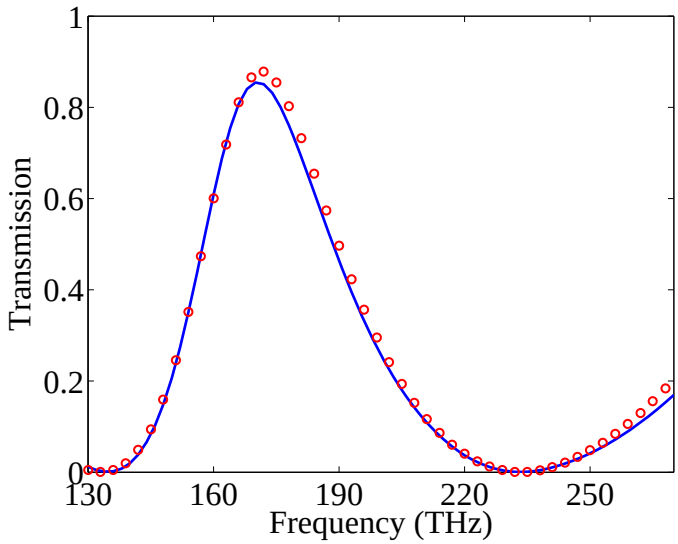

Fig. 3. Transmission response $T_{\mathrm{FDFD}}(L_1^{(1)}, L_2^{(1)})$ of the structure of Fig. 1(a) calculated with FDFD (solid line) for parameters obtained after the first iteration of the space mapping algorithm. We also show the coarse transmission line model response $T_{\mathrm{TL}}(L_{\mathrm{TL1}}^{(1)}, L_{\mathrm{TL2}}^{(1)})$ (circles), where $L_{\mathrm{TL1}}^{(1)}$, $L_{\mathrm{TL2}}^{(1)}$ are obtained through the parameter extraction procedure described in Subsection 2.2 .

transmission response of the device $T_{\mathrm{FDFD}}(L_1^{(j)}, L_2^{(j)})$ after the jth iteration calculated with the fine FDFD model. The device response from the initial step of the algorithm $T_{\mathrm{FDFD}}(L_1^{(1)}, L_2^{(1)})$, which as mentioned above is obtained from the optimal solution of the coarse transmission line model, does not meet the desired specifications. The device response obtained after the second iteration $T_{\mathrm{FDFD}}(L_1^{(2)}, L_2^{(2)})$ satisfies the specifications in almost the entire frequency range (Fig. 2). Finally, after the third iteration the transmission response of the device $T_{\mathrm{FDFD}}(L_1^{(3)}, L_2^{(3)})$ calculated with the fine FDFD model satisfies the specifications in the entire frequency range (Fig. 2). Thus, in this example the space mapping algorithm results in a device which satisfies all the design specifications after only 3 iterations. In other words, full-wave FDFD simulations of only 3 candidate structures are required before the iterative process is terminated. Use of the space mapping algorithm therefore results in large reductions in the required computation time when compared to any direct optimization method of the fine FDFD model.

At each iteration of the space mapping algorithm, we use the parameter extraction procedure described in Subsection 2.2 to obtain the mapping which corresponds to the optimum match between the coarse transmission line and fine FDFD model responses. The objective function H to be minimized during the parameter extraction [Eq. (15)] is based on the model responses at 15 frequency points from 130 THz to 270 THz with a step of 10 THz. In Fig. 3 we show the device response from the initial step of the algorithm $T_{\mathrm{FDFD}}(L_1^{(1)}, L_2^{(1)})$ (solid line). Using the parameter extraction procedure, we obtain the mapping $[L_{\mathrm{TL1}}^{(1)} \quad L_{\mathrm{TL2}}^{(1)}]^T = \mathbf{P}([L_1^{(1)} \quad L_2^{(1)}]^T) = [238 \text{ nm} \quad 419 \text{ nm}]^T$. In Fig. 3 we also show the corresponding coarse transmission line model response $T_{\mathrm{TL}}(L_{\mathrm{TL1}}^{(1)}, L_{\mathrm{TL2}}^{(1)})$ (circles). We observe that there is very good agreement between the device response $T_{\mathrm{FDFD}}(L_1^{(1)}, L_2^{(1)})$ and the transmission line model response $T_{\mathrm{TL}}(L_{\mathrm{TL1}}^{(1)}, L_{\mathrm{TL2}}^{(1)})$ ob-

#200639 - $15.00 USD Received 4 Nov 2013; revised 5 Dec 2013; accepted 10 Dec 2013; published 18 Dec 2013

tained through the parameter extraction procedure in the entire frequency range. This demonstrates that a mapping $\mathbf{P}$ that relates the fine FDFD and the coarse transmission line model parameters through $\mathbf{L}_{\mathrm{TL}} = \mathbf{P}(\mathbf{L})$ can indeed be established such that $T_{\mathrm{TL}}(\mathbf{P}(\mathbf{L})) \simeq T_{\mathrm{FDFD}}(\mathbf{L})$ in the frequency range of interest. It is the existence of such a one-to-one mapping that enables the space mapping algorithm to converge to a desired design after a few iterations. If a one-to-one mapping between the fine and coarse models cannot be established, the algorithm may fail to converge [15].

Table 1. The design parameters $L_1^{(j)}$, $L_2^{(j)}$ found after jth iteration of the space mapping algorithm for the structure of Fig. 1(a).

	$j=1$	$j=2$	$j=3$
$L_1^{(j)}$ (nm)	210	182	180
$L_2^{(j)}$ (nm)	384	349	351

3.2. MDM waveguide side-coupled to two arrays of MDM stub resonators

We next consider an example in which space mapping is applied to the design of a multicomponent nanoplasmonic device. The structure consists of a MDM plasmonic waveguide side-coupled to two arrays of MDM stub resonators [33] [Fig. 4(a)]. The fundamental TM mode of the MDM waveguide is incident from the left. As in the previous example, we wish to design a structure with a bandpass filter response. In the waveguide device geometry of Fig. 4(a) the use of multiple stubs can reduce the transmission in the stopbands. In addition, the use of two stub arrays with different stub lengths can result in narrower bandwidth of the passband [33]. In this case, the design specifications imposed on the transmission response T of the structure [indicated in Figs. 4(c) and 4(d) with solid red lines] are

$$T > 0.5 \quad \text{for} \quad 190\ \text{THz} < f < 200\ \text{THz}, \tag{22a}$$

$$T < 0.03 \quad \text{for} \quad 110\ \text{THz} < f < 160\ \text{THz} \quad \text{and} \quad 230\ \text{THz} < f < 290\ \text{THz}. \tag{22b}$$

Here the design parameters are the lengths of the stub resonators in the two arrays L_1 and L_2, as well as the distance L_3 between two adjacent stubs. The width w of all waveguide sections is fixed at $w = 50$ nm. The first and second array consist of 3 and 4 stubs, respectively.

Based on transmission line theory, the transmission line model of this structure consists of a transmission line with propagation constant γ and characteristic impedance Z loaded with two arrays of short-circuited transmission line stub resonators of lengths L_{TL1} and L_{TL2} with the same propagation constant γ and characteristic impedance Z [Fig. 4(b)]. The distance between two adjacent transmission line stub resonators is L_{TL3}. The characteristic impedance Z is given by Eq. (19). To obtain the transmission line model response of the structure $T_{\mathrm{TL}}(L_{\mathrm{TL1}}, L_{\mathrm{TL2}}, L_{\mathrm{TL3}})$, each of the MDM waveguide sections of the multicomponent device is modeled using a 2×2 transfer matrix [29, 34]. The overall transfer matrix is obtained by multiplying the transfer matrices of the individual components [29].

As in the previous example, the transmission line model of this structure is computationally efficient but its accuracy is limited. We use the coarse transmission line model of the structure (without space mapping) in combination with the genetic global optimization algorithm to find the transmission line model parameters L_{TL1}, L_{TL2}, and L_{TL3} such that the transmission line model response $T_{\mathrm{TL}}(L_{\mathrm{TL1}}, L_{\mathrm{TL2}}, L_{\mathrm{TL3}})$ satisfies the design specifications. The optimal transmission line model parameters found using this approach are $L^*_{\mathrm{TL1}} = 183$ nm, $L^*_{\mathrm{TL2}} = 466$ nm, and

#200639 - $15.00 USD Received 4 Nov 2013; revised 5 Dec 2013; accepted 10 Dec 2013; published 18 Dec 2013

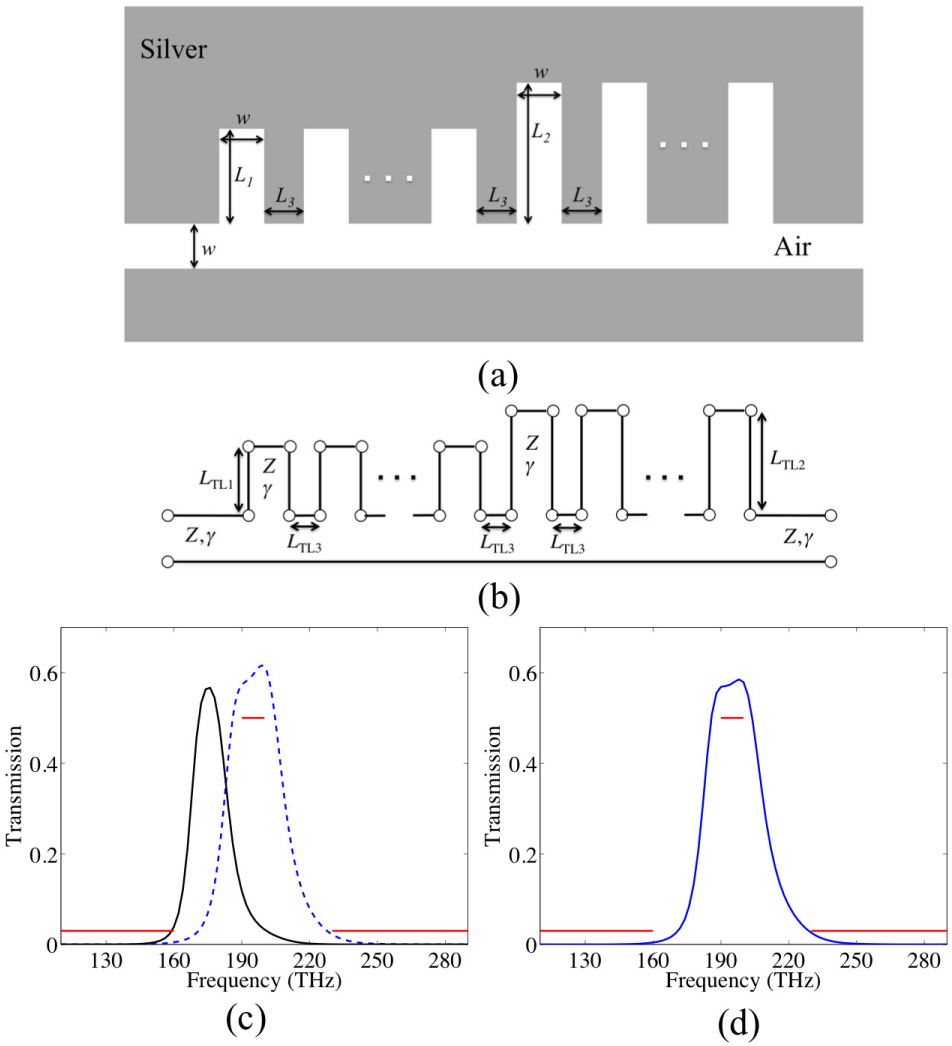

Fig. 4. (a) Schematic of a MDM plasmonic waveguide side-coupled to two arrays of MDM stub resonators. (b) Schematic of the transmission line model for the structure of Fig. 4(a). Here $Z(\omega)$ and $\gamma(\omega)$ are the characteristic impedance and complex propagation constant of the fundamental TM mode of a silver-air-silver plasmonic waveguide with width w. (c) Transmission line model response $T_{\rm TL}(L^*_{\rm TL1},L^*_{\rm TL2},L^*_{\rm TL3})$ of the structure of Fig. 4(a) for parameters $L^*_{\rm TL1}=183$ nm, $L^*_{\rm TL2}=466$ nm, and $L^*_{\rm TL3}=229$ nm obtained by optimizing the transmission line model of Fig. 4(b) (dashed blue line). We also show the transmission response calculated using FDFD, $T_{\rm FDFD}(L_1=L^*_{\rm TL1},L_2=L^*_{\rm TL2},L_3=L^*_{\rm TL3})$ for the same parameters (solid black line). Results are shown for $w=50$ nm. The red lines are the design specifications imposed on the transmission response of this structure. (d) Transmission response $T_{\rm FDFD}(\bar{L}_1,\bar{L}_2,\bar{L}_3)$ of the structure of Fig. 4(a) calculated with FDFD for the parameters $\bar{L}_1=159$ nm, $\bar{L}_2=439$ nm, and $\bar{L}_3=196$ nm obtained by the space mapping algorithm.

$L^*_{\rm TL3}=229$ nm. As shown in Fig. 4(c), the transmission line model response for the optimized device $T_{\rm TL}(L^*_{\rm TL1},L^*_{\rm TL2},L^*_{\rm TL3})$ (dashed blue line) meets all the design specifications [Eq. (22)].

#200639 - $15.00 USD Received 4 Nov 2013; revised 5 Dec 2013; accepted 10 Dec 2013; published 18 Dec 2013

As in the previous example, we investigate whether optimizing the transmission line model of the structure is enough to obtain a device which satisfies all the design specifications. We therefore perform a full-wave FDFD simulation of the device setting the design parameters L_1, L_2, L_3 equal to the optimal transmission line model parameters, and obtain the device response $T_{\text{FDFD}}(L_1 = L^*_{\text{TL1}}, L_2 = L^*_{\text{TL2}}, L_3 = L^*_{\text{TL3}})$. We observe that the transmission response of the device obtained with this approach $T_{\text{FDFD}}(L_1 = L^*_{\text{TL1}}, L_2 = L^*_{\text{TL2}}, L_3 = L^*_{\text{TL3}})$ (black solid line) is substantially different from the transmission line model response $T_{\text{TL}}(L^*_{\text{TL1}}, L^*_{\text{TL2}}, L^*_{\text{TL3}})$ (dashed blue line), and does not meet all the desired specifications [Fig. 4(c)]. This is due to the limited accuracy of the transmission line model which was discussed above. Thus, as in the previous example, simply optimizing the transmission line model of the device is not enough to obtain a device which satisfies all the required design specifications.

We therefore then use the space mapping algorithm (Section 2), to obtain a device which will satisfy all the design specifications. The objective function H to be minimized during the parameter extraction [Eq. (15)] is based on the coarse transmission line and fine FDFD model responses at 21 frequency points from 100 THz to 300 THz with a step of 10 THz. The design parameters $L_1^{(j)}$, $L_2^{(j)}$, $L_3^{(j)}$ found after the jth iteration of the algorithm are shown in Table 2. In this example the space mapping algorithm results in the design $\bar{L}_1 = 159$ nm, $\bar{L}_2 = 439$ nm, $\bar{L}_3 = 196$ nm, which satisfies all the design specifications [Fig. 4(d)], after only 3 iterations. Thus, as in the previous example, the use of the space mapping algorithm results in large reductions in the required computation time when compared to any direct optimization method of the fine FDFD model.

Table 2. The design parameters $L_1^{(j)}$, $L_2^{(j)}$, and $L_3^{(j)}$ found after jth iteration of the space mapping algorithm for the structure of Fig. 4(a).

	$j = 1$	$j = 2$	$j = 3$
$L_1^{(j)}$ (nm)	183	156	159
$L_2^{(j)}$ (nm)	466	439	439
$L_3^{(j)}$ (nm)	229	196	196

3.3. Two nanorods juxtaposed in parallel in a waveguide

We finally consider an example where space mapping is applied to the design of a nanoplasmonic device which includes deep subwavelength dielectric and metallic structures. Due to their deep subwavelength dimensions, these structures are modeled as lumped circuit elements rather than as transmission lines. In this example, the plasmonic device consists of a silicon ($\varepsilon_r = 14.15$) and a silver nanorod juxtaposed in parallel in a waveguide [35,36] [Fig. 5(a)]. The parallel-plate waveguide is bounded on top and bottom by perfect electric conductors (PEC), which represent an impenetrable metal with sufficiently negative permittivity in the frequency range of interest [36]. The nanorods are connected to a PEC protrusion attached to the bottom of the waveguide [Fig. 5(a)]. The fundamental TEM mode of the parallel-plate waveguide is incident from the left.

Here we wish to use the plasmonic waveguide device of Fig. 5(a), which is based on two optical lumped nanocircuit elements, to design a structure with a bandpass filter response. More specifically, the design specifications imposed on the transmission response T of the structure are

#200639 - $15.00 USD Received 4 Nov 2013; revised 5 Dec 2013; accepted 10 Dec 2013; published 18 Dec 2013

$$T > 0.36 \quad \text{for} \quad 330\ \text{THz} < f < 360\ \text{THz}, \tag{23a}$$

$$T < 0.18 \quad \text{for} \quad 120\ \text{THz} < f < 270\ \text{THz} \quad \text{and} \quad 420\ \text{THz} < f < 630\ \text{THz}. \tag{23b}$$

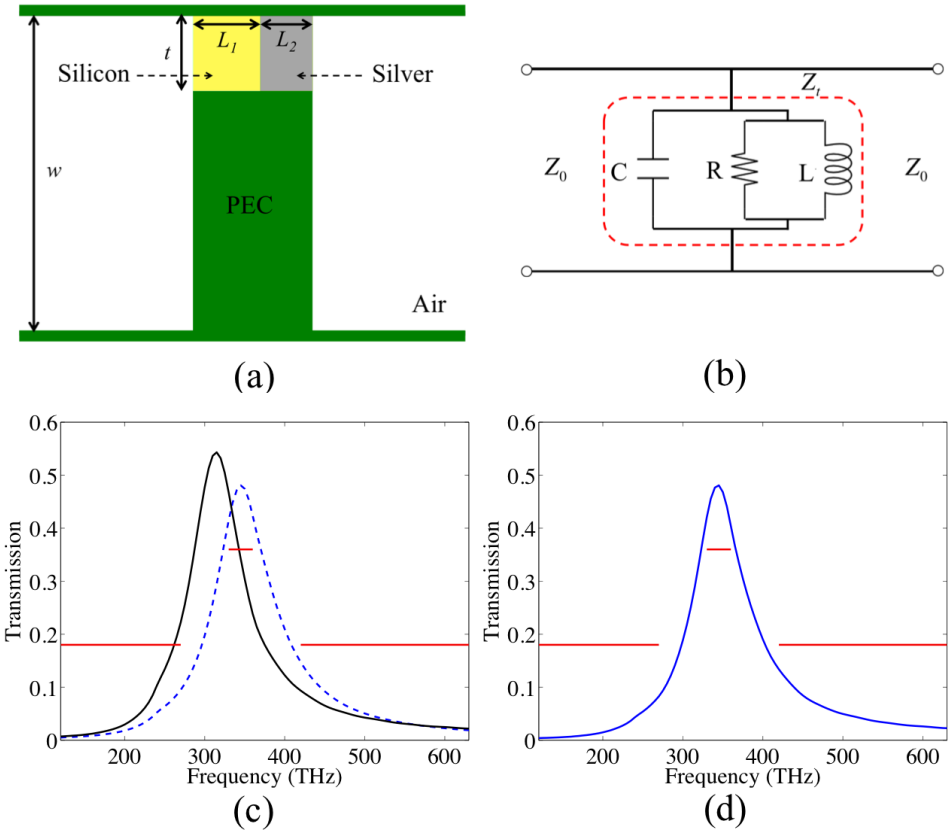

Fig. 5. (a) Schematic of a nanoplasmonic waveguide device consisting of a silicon and a silver nanorod juxtaposed in parallel in a waveguide. The parallel-plate waveguide is bounded on top and bottom by perfect electric conductors (PEC). The nanorods are connected to a PEC protrusion attached to the bottom of the waveguide. (b) Schematic of the transmission line model for the structure of Fig. 5(a). Here Z_0 is the characteristic impedance of the PEC parallel-plate waveguide. The shunt impedance Z_t consists of the parallel combination of a capacitor, a resistor, and an inductor. (c) Transmission line model response $T_{\text{TL}}(L^*_{\text{TL1}}, L^*_{\text{TL2}})$ of the structure of Fig. 5(a) for parameters $L^*_{\text{TL1}} = 20$ nm and $L^*_{\text{TL2}} = 7$ nm obtained by optimizing the transmission line model of Fig. 5(b) (dashed blue line). We also show the transmission response calculated using FDFD, $T_{\text{FDFD}}(L_1 = L^*_{\text{TL1}}, L_2 = L^*_{\text{TL2}})$ for the same parameters (solid black line). Results are shown for $w = 50$ nm and $t = 10$ nm. The red lines are the design specifications imposed on the transmission response of this structure. (d) Transmission response $T_{\text{FDFD}}(\bar{L}_1, \bar{L}_2)$ of the structure of Fig. 5(a) calculated with FDFD for the parameters $\bar{L}_1 = 20$ nm and $\bar{L}_2 = 9$ nm obtained by the space mapping algorithm.

The specifications are indicated in Figs. 5(c) and 5(d) with solid red lines. Here the design parameters are the lengths of the silicon and silver nanorods L_1 and L_2, while the width w of the waveguide and t of the nanorods are fixed at $w = 50$ nm and $t = 10$ nm, respectively.

#200639 - $15.00 USD Received 4 Nov 2013; revised 5 Dec 2013; accepted 10 Dec 2013; published 18 Dec 2013

As mentioned above, the nanorods can be modeled as lumped circuit elements [36]. More specifically, since the dielectric constant of silicon is real and positive, the silicon nanorod is modeled as a lumped capacitor with a capacitance per unit length given by [36]

$$C = \varepsilon_0 \varepsilon_r \frac{L_1}{t}. \tag{24}$$

In addition, since the real part of the dielectric constant of silver is negative in the frequency range of interest, the silver nanorod is modeled as a lumped inductor in parallel to a lumped resistor. Here the resistor accounts for the material losses in the silver nanorod. The inductance and resistance per unit length are associated with the real and imaginary parts of the dielectric constant of silver, respectively, and are given by [36]

$$L = -\frac{t}{\omega^2 \mathrm{Re}(\varepsilon_m) L_2}, \tag{25}$$

$$R = \frac{t}{\omega \mathrm{Im}(\varepsilon_m) L_2}, \tag{26}$$

where ε_m is the dielectric permittivity of silver. Thus, overall the silicon and silver nanorods are equivalent to the parallel combination of a resistor, an inductor, and a capacitor. The transmission line model of the waveguide device of Fig. 5(a) therefore consists of a shunt impedance Z_t coupled in parallel to a transmission line with characteristic impedance Z_0 [Fig. 5(b)]. Here the shunt impedance is given by

$$Z_t = (Z_C^{-1} + R^{-1} + Z_L^{-1})^{-1} = [j\omega C + R^{-1} + (j\omega L)^{-1}]^{-1}, \tag{27}$$

while the characteristic impedance of the PEC parallel-plate waveguide is [26]

$$Z_0 = \sqrt{\frac{\mu_0}{\varepsilon_0}} w. \tag{28}$$

Based on transmission line theory, the transmission line model response $T_{\mathrm{TL}}(L_{\mathrm{TL1}}, L_{\mathrm{TL2}})$ of the structure of Fig. 5(a) can be calculated as [26]

$$T_{\mathrm{TL}} = \left| \frac{2Z_t}{2Z_t + Z_0} \right|^2. \tag{29}$$

As in the previous examples, we first use the coarse transmission line model of the structure (without space mapping) in combination with the genetic global optimization algorithm to find the nanorod lengths L_{TL1} and L_{TL2} such that the transmission line model response $T_{\mathrm{TL}}(L_{\mathrm{TL1}}, L_{\mathrm{TL2}})$ satisfies the design specifications. The optimal transmission line model nanorod lengths found using this approach are $L^*_{\mathrm{TL1}} = 20$ nm and $L^*_{\mathrm{TL2}} = 7$ nm. As shown in Fig. 5(c), the transmission line model response for the optimized device $T_{\mathrm{TL}}(L^*_{\mathrm{TL1}}, L^*_{\mathrm{TL2}})$ (dashed blue line) meets all the design specifications [Eq. (23)]. As in previous examples, we then investigate whether optimizing the transmission line model of the structure is enough to obtain a device which satisfies all the design specifications. We therefore perform a full-wave FDFD simulation of the device setting the nanorod lengths L_1, L_2 equal to the optimal transmission line model nanorod lengths, and obtain the device response $T_{\mathrm{FDFD}}(L_1 = L^*_{\mathrm{TL1}}, L_2 = L^*_{\mathrm{TL2}})$. We observe that the transmission response of the device obtained with this approach $T_{\mathrm{FDFD}}(L_1 = L^*_{\mathrm{TL1}}, L_2 = L^*_{\mathrm{TL2}})$ (black solid line) is different from the transmission line model response $T_{\mathrm{TL}}(L^*_{\mathrm{TL1}}, L^*_{\mathrm{TL2}})$ (dashed blue line), and does not meet all the desired specifications [Fig. 5(c)]. This is due to the limited accuracy of the transmission line model. Thus, similarly

#200639 - $15.00 USD Received 4 Nov 2013; revised 5 Dec 2013; accepted 10 Dec 2013; published 18 Dec 2013

to the previous examples, simply optimizing the transmission line model of the device is not enough to obtain a device which satisfies all the required design specifications.

We therefore use the space mapping algorithm (Section 2), to obtain a device which will satisfy all the design specifications. As in the previous examples, the space mapping algorithm converges fast to the design $\bar{L}_1 = 20$ nm and $\bar{L}_2 = 9$ nm, which meets all the specifications [Fig. 5(d)]. In this case, the objective function H to be minimized during the parameter extraction [Eq. (15)] is based on the coarse transmission line and fine FDFD model responses at 18 frequency points from 120 THz to 630 THz with a frequency step of 30 THz. The design parameters $L_1^{(j)}$ and $L_2^{(j)}$ found after the jth iteration of the algorithm are shown in Table 3. In this case, only 2 iterations were required for the algorithm to converge to a design satisfying all the specifications. Thus, as in the previous examples, the use of the space mapping algorithm results in large reductions in the required computation time when compared to any direct optimization method of the fine FDFD model.

Table 3. The design parameters $L_1^{(j)}$, $L_2^{(j)}$ found after jth iteration of the space mapping algorithm for the structure of Fig. 5(a).

	$j=1$	$j=2$
$L_1^{(j)}$ (nm)	20	20
$L_2^{(j)}$ (nm)	7	9

4. Conclusions

In this paper, we showed that the space mapping algorithm, originally developed for microwave circuit optimization, can enable the efficient design of nanoplasmonic devices which satisfy a set of desired specifications. Space mapping utilizes a physics-based coarse model to approximate a fine model accurately describing a device.

More specifically, we demonstrated the use of the space mapping algorithm for the design of MDM plasmonic waveguide devices. A set of desired specifications are imposed on the transmission response of the device. The goal is to find the design parameters of the device so that its transmission response satisfies all the specifications. In our case, the fine model was a full-wave FDFD simulation of the device, while the coarse model was based on transmission line theory. We used the aggressive space mapping implementation of the algorithm, which incorporates a quasi-Newton iteration. At each iteration of the space mapping algorithm we used a parameter extraction procedure to obtain the mapping which corresponds to the optimum match between the coarse and fine model responses. The iterative procedure was terminated when the fine model response satisfied the set of desired specifications.

We considered several examples of the application of the space mapping algorithm for the design of nanoplasmonic waveguide devices. In the first example, we considered a plasmonic MDM waveguide side-coupled to two MDM stub resonators. The transmission line model of this structure consists of two short-circuited transmission line resonators, which are connected in series to a transmission line. In the second example, space mapping was applied to the design of a multicomponent nanoplasmonic device consisting of a MDM plasmonic waveguide side-coupled to two arrays of MDM stub resonators. The transmission line model in this case consists of a transmission line loaded with two arrays of short-circuited transmission line stub resonators. The model was implemented using the transfer matrix of each waveguide section. Finally, in the third example, space mapping was applied to the design of a nanoplasmonic waveguide device consisting of deep subwavelength dielectric and metallic structures. These structures were modeled as lumped circuit elements rather than as transmission lines.

#200639 - $15.00 USD Received 4 Nov 2013; revised 5 Dec 2013; accepted 10 Dec 2013; published 18 Dec 2013

Through these three examples, we showed that simply optimizing the transmission line model of the device is not enough to obtain a device which satisfies all the required design specifications. On the other hand, we found that, when the iterative space mapping algorithm was used, it converged fast to a design which met all the specifications. In addition, full-wave FDFD simulations of only a few candidate structures were required before the iterative process was terminated. Use of the space mapping algorithm therefore resulted in large reductions in the required computation time when compared to any direct optimization method of the fine FDFD model.

As final remarks, the use of more detailed transmission line models for nanoplasmonic waveguides [37, 38] in the space mapping algorithm could potentially further reduce the required number of full-wave simulations during the design process. While here we considered examples where space mapping is applied to the design of bandpass filters, the algorithm performs equally well when applied to the design of bandstop, lowpass, or highpass filters [15, 16, 39]. In addition, we note that the space mapping algorithm can also be applied to design three-dimensional nanoplasmonic waveguide devices, using as coarse models the transmission line models which have been developed for such waveguides [40]. The algorithm has already been successfully applied to design a variety of three-dimensional microwave waveguide devices [15, 16]. Finally, space mapping could also be employed to design a variety of other nanoplasmonic structures and devices, such as arrays of holes in metallic films, metallic gratings, and metallic nanoparticle arrays, using the analytical or quasi-analytical physics-based models which have been developed for such structures.

Acknowledgments

This research was supported by the Louisiana Board of Regents (contracts LEQSF(2009-12)-RD-A-08 and LEQSF-EPS(2012)-PFUND-281), and the National Science Foundation (Award No. 1254934).

#200639 - $15.00 USD Received 4 Nov 2013; revised 5 Dec 2013; accepted 10 Dec 2013; published 18 Dec 2013